

# FADTI: Fourier and Attention Driven Diffusion for Multivariate Time Series Imputation

Runze Li , Hanchen Wang , Wenjie Zhang , Binghao Li , Yu Zhang , Xuemin Lin , and Ying Zhang 

**Abstract**—Multivariate time series imputation is fundamental in applications such as healthcare, traffic forecasting, and biological modeling, where sensor failures and irregular sampling lead to pervasive missing values. However, existing Transformer- and diffusion-based models lack explicit inductive biases and frequency awareness, limiting their generalization under structured missing patterns and distribution shifts. We propose FADTI, a diffusion-based framework that injects frequency-informed feature modulation via a learnable Fourier Bias Projection (FBP) module and combines it with temporal modeling through self-attention and gated convolution. FBP supports multiple spectral bases, enabling adaptive encoding of both stationary and non-stationary patterns. This design injects frequency-domain inductive bias into the generative imputation process. Experiments on multiple benchmarks, including a newly introduced biological time series dataset, show that FADTI consistently outperforms state-of-the-art methods, particularly under high missing rates. Code is available at <https://anonymous.4open.science/r/TimeSeriesImputation-52BF>

**Index Terms**—Time series imputation, diffusion model, Fourier transform, frequency-domain modeling, attention mechanism

## I. INTRODUCTION

Multivariate time series imputation (MTSI) is critical in domains such as healthcare, finance, Internet of Things (IoT), and transportation [1]–[6]. In these scenarios, missing data arise from hardware or communication failures and from constraints on data collection. Sensor faults and system downtime in IoT, financial, and traffic systems create long gaps and irregular readings [4]–[6], while irregular sampling and privacy constraints substantially limit clinical data acquisition [7]–[9]. Such missing values can severely degrade downstream tasks such as forecasting, risk assessment, and decision making, making accurate imputation essential.

Runze Li and Wenjie Zhang are with the School of Computer Science and Engineering, University of New South Wales, Sydney, NSW 2052, Australia (e-mail: runze.li1@unsw.edu.au; wenjie.zhang@unsw.edu.au).

Hanchen Wang is with the University of Technology Sydney, Sydney, NSW 2007, Australia (e-mail: hanchen.wang@uts.edu.au).

Binghao Li is with the School of Minerals and Energy Resources Engineering, University of New South Wales, Sydney, NSW 2052, Australia (e-mail: binghao.li@unsw.edu.au).

Yu Zhang is with the School of Business, University of New South Wales, Canberra, ACT 2600, Australia (e-mail: m.yuzhang@unsw.edu.au).

Xuemin Lin is with the Antai College of Economics and Management, Shanghai Jiao Tong University, Shanghai 200240, China (e-mail: xuemin.lin@sjtu.edu.cn).

Ying Zhang is with the Common Prosperity Visualization and Policy Simulation Lab, Zhejiang Gongshang University, Hangzhou 310018, China (e-mail: ying.zhang@zjgsu.edu.cn).

This work has been submitted to the IEEE for possible publication. Copyright may be transferred without notice, after which this version may no longer be accessible.

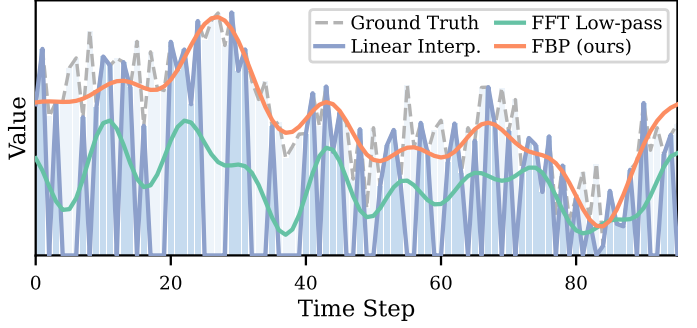


Fig. 1. Distortion of frequency-domain representations under missing values. The naive projection of masked series (green) shows attenuated and oversmoothed spectra compared to the ground truth (gray dashed), whereas our bias projection (orange) better preserves the true spectral structure.

Recent advances in MTSI have explored Transformer-based attention mechanisms and diffusion probabilistic models. Transformer-based models, exemplified by SAITS and its variants [10]–[13] and by TimesNet [14], capture long-range temporal dependencies via self-attention and model global context across time steps and variables. However, these models struggle to represent the uncertainty induced by high missing rates or ambiguous contexts, which is critical for robust imputation. In parallel, diffusion models have emerged as a powerful class of generative methods for conditional time series imputation [15]–[18]. They iteratively denoise samples drawn from a known noise distribution, offering principled uncertainty modeling, stable training, and support for arbitrary missing patterns through conditioning. Recent diffusion-based models, such as CSDI [19], MTSCI [20], and CSBI [21], achieve strong empirical performance across diverse benchmarks. However, several key challenges remain: (1) **Failure to capture structured frequency patterns.** Most existing methods lack explicit modeling of periodic or trend components, and thus struggle to recover long-term or repetitive temporal structures. (2) **Poor performance under sparse or irregular missingness.** Under sparse or long-range gaps, existing models often fail due to the absence of global cues such as frequency or trend continuity. (3) **Limited generalization.** Without structural assumptions (e.g., smoothness, periodicity), models struggle to generalize under data scarcity or distribution shift.

Time series often exhibit periodic or structured variations that are more clearly expressed in the frequency domain. Recent efforts integrate frequency-aware representations into time series models for forecasting and classification, such as TimesNet [14], FGFI [22], PSW-I [23] and TSLANet [24]. These methods, however, are rarely applied to imputation. They typically rely on fixed, non-learnable transforms and treat frequency features as static, detached from the temporal

modeling pipeline. As shown in Figure 1, directly projecting masked time series into the frequency domain produces distorted spectra that fail to recover the true patterns. This distortion arises because masking corrupts the global frequency structure, leading to energy loss and frequency misalignment. This yields three key limitations: (1) **Non-adaptive frequency transforms.** Fixed transforms cannot adjust to data-specific spectral characteristics. (2) **Lack of temporal alignment.** Frequency features are often global and cannot be naturally fused with temporal attention. (3) **Sensitivity to missingness.** Frequency transforms assume fully observed inputs and are highly sensitive to interpolation or zero-padding. Consequently, frequency-based modules are rarely applied in imputation, where missingness directly affects spectral estimation. As illustrated in Figure 1, our learnable bias projection is designed to mitigate these distortions.

Despite recent progress, existing models still lack a framework that effectively combines the complementary strengths of attention mechanisms, diffusion-based generative modeling, and frequency-domain representations. Most methods use only one or two of these components, limiting their expressiveness on real-world sequences with complex dynamics and diverse missing patterns. To address this gap, we propose a novel frequency-aware architecture centered around the **Fourier Bias Projection (FBP)** module. FBP injects frequency-domain inductive biases into the denoising diffusion process, improving the model’s ability to capture stationary and non-stationary components. In particular, FBP learns a time-dependent spectral bias and projects it onto low-frequency Fourier bands, so that it acts as a smooth global trend field rather than memorizing local fluctuations. This makes FBP particularly suitable for modeling long-term trends in multivariate time series. The modular design can be instantiated with standard Fourier-based transforms, including the Discrete Fourier Transform (DFT) [25], [26], Short-Time Fourier Transform (STFT) [27], and Fourier Synchro-squeezed Transform (FrSST) [28]. We further provide tailored STFT and FrSST implementations within FBP and apply them to MTSI for the first time.

Around this core module, we build a flexible architecture that integrates Transformer-based attention, conditional diffusion modeling, and optional gated convolution for modeling local temporal dependencies. Concretely, self-attention models long-range temporal and cross-variable dependencies from partially observed inputs, while the diffusion backbone models the conditional distribution of missing segments and provides calibrated uncertainty estimates. The proposed frequency-domain bias projection supplies global trend and periodic constraints that are hard to learn purely in the time domain. By coupling these three components within a single denoising pipeline, our model can simultaneously exploit local and global temporal structure, account for multimodal uncertainty under severe missingness, and enforce spectrally consistent imputations that are robust to sparse or irregular gaps.

The main contributions of this work are as follows:

- We propose a diffusion-based framework for MTSI that integrates frequency-domain information via a flexible FBP module, enabling adaptive encoding of both stationary and non-stationary components.

- We instantiate FBP with three Fourier-based transforms (DFT, STFT, and FrSST) and analyze their integration and efficiency within the framework.
- We incorporate a gated convolutional module into the temporal encoder for efficient local dependency modeling and reduced attention cost.
- We introduce a new dataset for complex, non-stationary environments, and extensive experiments across multiple benchmarks show that our model consistently outperforms state-of-the-art methods in accuracy and robustness under various missing settings.

## II. RELATED WORK

### A. Traditional Methods

Early statistical imputation methods rely on simple statistics such as zero, mean, or median imputation, or on classical statistical models [29], [30]. Traditional machine learning techniques such as regression, K-nearest neighbors (KNN), and matrix factorization have also been used for MTSI [31]–[34]. While statistical and classical machine learning methods are simple and computationally efficient, they often fail to capture complex temporal dependencies and dynamic patterns, which limits their imputation performance [35]. In this work, we focus instead on high-dimensional, nonstationary multivariate sequences with severe and irregular missingness.

### B. Predictive Methods

RNN-based models were among the first applied to MTSI, benefiting from sequential processing and time-aware decay mechanisms [1], [2], [36], [37]. However, their sequential nature and memory bottlenecks limit scalability on long sequences [38], [39]. CNN-based methods offer efficient local modeling but are inherently limited in capturing long-term dependencies due to fixed receptive fields [40]; they are often combined with spectral transforms such as the fast Fourier transform (FFT) or integrated into hybrid architectures to enhance temporal representation [14], [19], [41], [42]. GNN-based models capture spatiotemporal dependencies by modeling time series as graphs [43], but their computational cost can hinder use in large-scale scenarios [44].

Transformer architectures [45]–[47] have become prominent in MTSI due to their parallelizable self-attention and ability to model global dependencies. Variants like SAITS [10], Impute-Former [48], and attention-enhanced GNNs [49], [50] improve performance by integrating temporal context and missingness-aware training strategies. Furthermore, self-attention has been adopted as the core component in denoising networks within diffusion-based imputation models [19], [51]–[53], enabling uncertainty-aware, high-fidelity reconstructions. Our model inherits the global-dependency modeling of Transformers but combines it with a diffusion backbone and frequency-domain priors to better cope with long-range gaps and severe sparsity.

### C. Generative Methods

Variational Autoencoders (VAEs) and Generative Adversarial Networks (GANs) are two major classes of generative models applied to MTSI. VAEs provide probabilistic modeling and

interpretable latent representations [40], [54], [55], but their expressive power is often limited, leading to underestimation of complex variability. GANs generate realistic samples by adversarial training between a generator and discriminator [38], [56]. They can yield high-fidelity imputations but are difficult to train due to instability issues such as vanishing gradients and mode collapse [57], and enforcing temporal consistency in generated sequences remains challenging.

Diffusion models have gained traction for MTSI by modeling data through a progressive noising and denoising process [58]. CSDI [19] introduced conditional diffusion for multivariate time series imputation, achieving strong performance by conditioning on partial observations. However, its dual-Transformer denoising architecture incurs quadratic computational cost with respect to both variable count and sequence length, limiting scalability. To alleviate this, SSSD [59] replaces Transformers with structured state space models (SSMs) for improved efficiency, while CSBI [21] reformulates imputation as a Schrödinger bridge problem to enhance theoretical tractability. Recent variants such as SADI [60], MTSCI [20], PriSTI [53], and FGTI [22] further improve performance by incorporating temporal attention, cross-channel reasoning, contextual conditioning, and spectral cues. We follow this generative line by adopting a diffusion backbone and introducing a learnable Fourier bias that explicitly regularizes long-term trends and periodic components during denoising.

#### D. Fourier-based Time-Frequency Analysis

Time-frequency analysis (TFA) offers a powerful framework for representing nonstationary signals in the joint time-frequency domain, and the DFT and its short-time variant STFT are widely adopted in modern time series modeling due to their computational simplicity and compatibility with neural architectures [27]. STFT introduces a sliding window to capture localized frequency information, making it suitable for signals with moderate time-varying characteristics. However, its resolution is fundamentally constrained by the fixed window size, resulting in a trade-off between time and frequency localization [61]. To overcome these limitations, recent work has explored fractional Fourier transform (FrFT) variants, which generalize the classical Fourier transform by introducing a fractional order  $\alpha$  [62], [63]. FrSST refines FrFT by reassigning time-frequency energy along more accurate instantaneous frequency trajectories, combining the localization benefits of Synchrosqueezed Transform (SST) [64] with the tunability of FrFT to improve concentration and reconstruction for strongly nonstationary signals [28]. Unlike prior work that mainly applies these transforms to forecasting or classification with fully observed inputs, we embed DFT, STFT, and FrSST into an end-to-end Fourier Bias Projection module tailored for imputation under missingness.

### III. PRELIMINARIES

#### A. Problem Definition

*Definition 3.1 (Multivariate Time Series (MTS)):* An MTS is a sequence of  $D$ -dimensional real-valued vectors observed

at  $T$  discrete time steps, denoted by  $\mathbf{x} \in \mathbb{R}^{T \times D}$ , where  $\mathbf{x}[t, d]$  is the value of the  $d$ -th variable at time step  $t$ .

*Problem 3.1 (Multivariate Time Series Imputation (MTSI)):* Let  $\mathbf{x} \in \mathbb{R}^{T \times D}$  be an MTS with missing entries, and let  $\mathbf{m} \in \{0, 1\}^{T \times D}$  be a binary mask such that  $\mathbf{m}[t, d] = 1$  if  $\mathbf{x}[t, d]$  is observed and  $\mathbf{m}[t, d] = 0$  otherwise. The goal of MTSI is to estimate the missing values and recover a complete time series  $\hat{\mathbf{x}} \in \mathbb{R}^{T \times D}$  satisfying  $\hat{\mathbf{x}}[t, d] \approx \mathbf{x}[t, d]$  for all  $(t, d)$  with  $\mathbf{m}[t, d] = 0$ . Denote the missing values as  $\mathbf{x}^{\text{ta}}$ . The imputation task can be formulated as point estimation:

$$\min_{\theta} \mathbb{E} \left[ \left\| \hat{\mathbf{x}}^{\text{ta}} - \mathbf{x}^{\text{ta}} \right\|_2^2 \right]. \quad (1)$$

Compared with univariate imputation, MTSI must jointly model complex inter-variable dependencies and heterogeneous dimension-specific missingness patterns, which makes the problem more ill-posed but also enables information sharing across correlated variables.

#### B. Diffusion Models

Diffusion probabilistic models are generative models that define a Markovian forward noising process and a learned reverse denoising process [65], [66].

1) *Forward Process:* Let  $\mathbf{x}_0 \in \mathbb{R}^{T \times D}$  be a data sample drawn from an unknown data distribution  $q(\mathbf{x}_0)$ . The forward process constructs a sequence of latent variables  $\{\mathbf{x}_1, \dots, \mathbf{x}_S\}$  by gradually adding Gaussian noise to the data over  $S$  steps, following a Markov chain:

$$\begin{aligned} q(\mathbf{x}_{1:S} \mid \mathbf{x}_0) &:= \prod_{s=1}^S q(\mathbf{x}_s \mid \mathbf{x}_{s-1}), \\ q(\mathbf{x}_s \mid \mathbf{x}_{s-1}) &:= \mathcal{N}(\sqrt{\alpha_s} \mathbf{x}_{s-1}, (1 - \alpha_s) \mathbf{I}), \end{aligned} \quad (2)$$

where  $\{\alpha_s\}_{s=1}^S \subset (0, 1)$  is a predefined noise schedule. The marginal distribution at any step  $s$  then has the closed form

$$q(\mathbf{x}_s \mid \mathbf{x}_0) := \mathcal{N}(\sqrt{\bar{\alpha}_s} \mathbf{x}_0, (1 - \bar{\alpha}_s) \mathbf{I}), \quad \bar{\alpha}_s := \prod_{i=1}^s \alpha_i. \quad (3)$$

This allows sampling of  $\mathbf{x}_s$  from  $\mathbf{x}_0$  as

$$\mathbf{x}_s = \sqrt{\bar{\alpha}_s} \mathbf{x}_0 + \sqrt{1 - \bar{\alpha}_s} \boldsymbol{\epsilon}, \quad \boldsymbol{\epsilon} \sim \mathcal{N}(\mathbf{0}, \mathbf{I}). \quad (4)$$

2) *Reverse Process:* The goal of the reverse process is to recover  $\mathbf{x}_0$  from noisy observations  $\mathbf{x}_S$ . It is modeled by a parameterized Markov chain:

$$p_{\theta}(\mathbf{x}_{0:S}) := p(\mathbf{x}_S) \prod_{s=1}^S p_{\theta}(\mathbf{x}_{s-1} \mid \mathbf{x}_s), \quad (5)$$

where  $p(\mathbf{x}_S) = \mathcal{N}(\mathbf{0}, \mathbf{I})$  is a standard Gaussian prior, and each reverse transition is modeled as

$$p_{\theta}(\mathbf{x}_{s-1} \mid \mathbf{x}_s) := \mathcal{N}(\boldsymbol{\mu}_{\theta}(\mathbf{x}_s, s), \sigma_s^2 \mathbf{I}), \quad (6)$$

with a fixed variance schedule  $\{\sigma_s^2\}_{s=1}^S$ .

3) *Parameterization*: Ho et al. [66] proposed to parameterize  $\mu_\theta(\mathbf{x}_s, s)$  using a neural network  $\epsilon_\theta$  that predicts the noise added at step  $s$ :

$$\mu_\theta(\mathbf{x}_s, s) = \frac{1}{\sqrt{\alpha_s}} \left( \mathbf{x}_s - \frac{1 - \alpha_s}{\sqrt{1 - \bar{\alpha}_s}} \epsilon_\theta(\mathbf{x}_s, s) \right), \quad (7)$$

where  $\alpha_s$  and  $\bar{\alpha}_s$  are the same noise schedule coefficients as in the forward process. The model is trained by minimizing the following denoising score matching loss:

$$\mathcal{L}_{\text{simple}}(\theta) := \mathbb{E}_{\mathbf{x}_0, \epsilon, s} \|\epsilon - \epsilon_\theta(\mathbf{x}_s, s)\|^2. \quad (8)$$

This objective trains  $\epsilon_\theta$  to predict the noise  $\epsilon$  used in (4), thereby guiding the reverse process toward accurate reconstruction of  $\mathbf{x}_0$ .

### C. Imputation with Conditional Diffusion Models

While diffusion models are primarily designed for unconditional data generation, they can be naturally extended to probabilistic imputation tasks. Given a sample  $\mathbf{x}_0 \in \mathbb{R}^{T \times D}$ , we split it into observed part  $\mathbf{x}_0^{\text{co}}$  and missing part  $\mathbf{x}_0^{\text{ta}}$ , and aim to learn a model  $p_\theta(\mathbf{x}_0^{\text{ta}} \mid \mathbf{x}_0^{\text{co}})$  that approximates the true conditional distribution  $q(\mathbf{x}_0^{\text{ta}} \mid \mathbf{x}_0^{\text{co}})$ . To adapt diffusion models for conditional imputation, the reverse process, equation (5) and (6), is extended to:

$$p_\theta(\mathbf{x}_0^{\text{ta}} \mid \mathbf{x}_0^{\text{co}}) := p(\mathbf{x}_S^{\text{ta}}) \prod_{s=1}^S p_\theta(\mathbf{x}_{s-1}^{\text{ta}} \mid \mathbf{x}_s^{\text{ta}}, \mathbf{x}_0^{\text{co}}), \quad (9)$$

where  $\mathbf{x}_S^{\text{ta}} \sim \mathcal{N}(\mathbf{0}, \mathbf{I})$  denotes the standard Gaussian prior.

$$p_\theta(\mathbf{x}_{s-1}^{\text{ta}} \mid \mathbf{x}_s^{\text{ta}}, \mathbf{x}_0^{\text{co}}) := \mathcal{N}(\mu_\theta(\mathbf{x}_s^{\text{ta}}, s \mid \mathbf{x}_0^{\text{co}}), \sigma_s^2 \mathbf{I}), \quad (10)$$

where  $\mu_\theta$  is predicted by a neural network that takes both the current noisy input  $\mathbf{x}_s^{\text{ta}}$  and the conditional input  $\mathbf{x}_0^{\text{co}}$  as inputs.

Table I summarizes the main notation used in this paper.

## IV. METHODOLOGY

### A. Overview

To address the limitations of prior methods in modeling uncertainty under high missing rates, we propose a conditional diffusion model for multivariate time series imputation that combines frequency-informed modulation with feature-wise attention for better temporal and cross-variable consistency. Central to this framework is the **Fourier Bias Projection (FBP)** module, which injects learnable spectral priors into the denoising process to stabilize uncertainty-aware reconstruction. The overall architecture is illustrated in Figure 2.

1) *Modeling of Missing Values*: Let  $\mathbf{X} \in \mathbb{R}^{B \times T \times D}$  denote the input series and  $\mathbf{M} \in \{0, 1\}^{B \times T \times D}$  its binary observation mask, where  $B$  is the batch size. We apply the mask  $\mathbf{M}$  to obtain a corrupted input and then run a forward diffusion process that adds stepwise Gaussian noise along time to generate the noisy input. To guide the reverse diffusion process, the model incorporates two forms of conditioning information. First, a diffusion time-step embedding  $s \in \mathbb{R}^B$  provides temporal context for each reverse-diffusion step. Second, a conditional feature representation  $\mathbf{X}^{\text{cf}} \in \mathbb{R}^{B \times C^{\text{cf}} \times T \times D}$  is extracted from

TABLE I  
MAIN NOTATION USED IN THIS PAPER.

Symbol	Description
$\mathbf{x}, \hat{\mathbf{x}}$	Original / imputed MTS (single sample)
$\mathbf{m}$	Observation mask
$\mathbf{X}, \hat{\mathbf{X}}$	Original / imputed MTS (batch)
$\mathbf{M}, \mathbf{M}^{\text{co}}, \mathbf{M}^{\text{ta}}$	Observed / conditional / target masks
$\mathbf{X}^{\text{co}}$	Conditional part, $\mathbf{M}^{\text{co}} \odot \mathbf{X}$
$B, T, D, C$	Batch, time, variable, channel
$\mathbf{X}^{\text{trend}}, \mathbf{X}^{\text{res}}$	Trend / residual components
$\mathbf{X}^{\text{freq}}$	Frequency-domain features (FBP)
$\mathbf{X}^{\text{cf}}, C^{\text{cf}}$	Conditional features / channels
$K_d, K_f$	Decomposition kernel / spectral window
$F, L$	Frequency bins / time frames
$s, S$	Diffusion step / total steps
$\mathbf{x}_s$	Noisy sample at step $s$ (single sample)
$\mathbf{X}_s$	Noisy sample at step $s$ (batch)
$\mathbf{X}_s^{\text{ta}}, \mathbf{X}_S^{\text{ta}}$	Target inputs at step $s$ / initial noise
$\bar{\alpha}_s, \alpha_s, \sigma_s$	Noise schedule parameters
$\epsilon, \hat{\epsilon}$	True / predicted noise
$\zeta$	Sampling noise in reverse process
$K$	Number of samples for averaging

the observed entries by a conditional feature extraction module, where  $C^{\text{cf}}$  denotes the number of feature channels. These conditioning signals are injected into the residual denoising blocks to guide the reconstruction of missing entries.

The denoising backbone is a stack of residual blocks, each containing three modules: (1) **Temporal Frequency Module**, which combines FBP with attention or convolutional layers so that FBP contributes frequency-domain features for global temporal dependencies and the attention or convolutional layers model variable interactions; (2) **Feature Attention Module**, which applies variable-level attention to selectively focus on relevant variables during imputation; and (3) **Gated Filter Module**, which combines filtered and gated features to form the residual update at each step. Each residual block processes the noisy input together with the conditioning information and outputs an intermediate denoised estimate. The final representation is passed to a projection head to obtain the imputed series  $\hat{\mathbf{X}} \in \mathbb{R}^{B \times T \times D}$ , with missing values filled according to the learned conditional distributions.

### B. Fourier-Based Frequency-Aware Features

Time series often exhibit global patterns such as trends and periodicities, which can be more effectively represented in the frequency domain using frequency-based transformations [25]. Let  $F$  denote the number of selected frequency components, determining the frequency resolution (distinct from the number of time steps  $T$ ). Each frequency bin is indexed by  $f \in [0, F)$ . Given an input sequence  $\mathbf{X}$ , we apply a frequency transform along the temporal axis to extract frequency-aware features:

$$\tilde{\mathbf{X}} = \mathcal{F}(\mathbf{X}), \quad \tilde{\mathbf{X}} \in \mathbb{C}^{F \times D}. \quad (11)$$

Here,  $\mathcal{F}(\cdot)$  denotes a transform instantiated by classical frequency-domain operators such as DFT, STFT, and

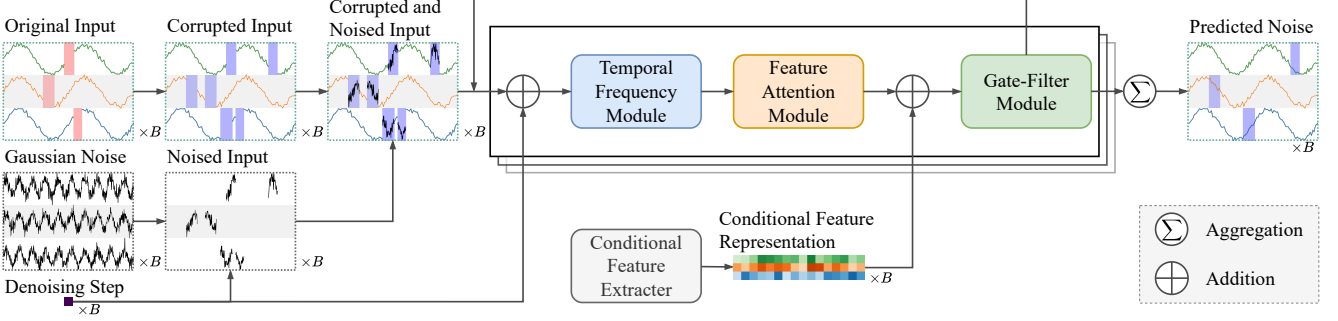


Fig. 2. Overview of the FADTI framework. The model performs denoising-based imputation via conditional feature extraction, temporal–frequency modeling, and gated attention, predicting and removing noise from corrupted inputs to reconstruct the imputed time series.

FrSST [25]–[28]. We implement all three transforms within the FBP module and, to the best of our knowledge, apply STFT and FrSST to multivariate time series imputation for the first time. We denote  $K$  as the window length used for spectral transforms, representing the number of time steps involved in each frequency decomposition.

1) *Discrete Fourier Transform (DFT)*: Projects the entire sequence into the frequency domain globally, assuming stationarity and lacking temporal localization:

$$\tilde{\mathbf{X}}^{\text{DFT}}[d, f] = \sum_{k=0}^{K-1} \mathbf{X}[d, k] \cdot e^{-2\pi i f k / K}, \quad K = T. \quad (12)$$

In our implementation, we compute DFT via rFFT to obtain a complex-valued representation:

$$\tilde{\mathbf{X}}^{\text{DFT}} = \text{rFFT}(\mathbf{X}), \quad \tilde{\mathbf{X}}^{\text{DFT}} \in \mathbb{R}^{B \times D \times C \times F}. \quad (13)$$

We then normalize it as

$$\text{Normalization}(\tilde{\mathbf{X}}^{\text{DFT}}) = \frac{2}{T} \cdot \tilde{\mathbf{X}}^{\text{DFT}}. \quad (14)$$

DFT provides global spectral encoding, capturing overall trends and periodicities with high precision, and is effective for smooth and stable global patterns such as stationary or highly periodic sequences (e.g., traffic flow, climate data).

2) *Short-Time Fourier Transform (STFT)*: Introduces a sliding window to provide localized frequency analysis:

$$\tilde{\mathbf{X}}^{\text{STFT}}[d, \tau, f] = \sum_{k=0}^{K-1} \mathbf{X}[d, k] \cdot w(k - \tau) \cdot e^{-2\pi i f k / K}, \quad (15)$$

where  $w(\cdot)$  is a window function centered at  $\tau$ . This enables a trade-off between time and frequency resolution, but suffers from fixed resolution limitations. In our implementation, the input  $\mathbf{X}$  is segmented into overlapping windows, and a  $K_f$ -point DFT is applied to each segment, yielding a localized time–frequency representation:

$$\tilde{\mathbf{X}}^{\text{STFT}} = \text{STFT}(\mathbf{X}, K_f, \frac{K_f}{2}, w(\cdot)), \quad \tilde{\mathbf{X}}^{\text{STFT}} \in \mathbb{R}^{B \times D \times C \times F \times L}, \quad (16)$$

where  $\frac{K_f}{2}$  is the frame stride, which is  $\tau_{i+1} - \tau_i$ . We set the FFT window length to  $K_f = \frac{2}{3}T$ , and use the Hann window for  $w(\cdot)$ . The normalization is

$$E_w = \sum_{k=0}^{K_f-1} w(k)^2, \quad \text{Normalization}(\tilde{\mathbf{X}}^{\text{STFT}}) = \frac{1}{E_w} \cdot \tilde{\mathbf{X}}^{\text{STFT}}. \quad (17)$$

STFT employs a sliding window for localized time–frequency analysis, enabling simultaneous capture of local temporal features and frequency variations, and is particularly suitable for non-stationary sequences with short-term dynamics (e.g., financial time series, medical monitoring).

3) *Fourier-based Synchrosqueezing Transform (FrSST)*: Classical FrSST is derived in the short-time fractional Fourier transform (STFrFT) domain by modeling each analytic component as a locally linear chirp and then synchrosqueezing the STFrFT energy along the fractional-frequency axis according to an instantaneous-frequency estimator. Here we adopt its Fourier-based instantiation, where STFrFT reduces to the standard STFT and the synchrosqueezing acts directly on the STFT coefficients:

$$\tilde{\mathbf{X}}^{\text{FrSST}}[d, \tau, \xi] = \int \tilde{\mathbf{X}}^{\text{STFT}}[d, \tau, f] \cdot \delta(\xi - \omega(\tau, f)) df, \quad (18)$$

where  $\omega(\tau, f)$  denotes the instantaneous frequency derived from the phase of the STFT. This yields sharper frequency localization and better captures non-stationary dynamics. In our implementation, we first compute the standard STFT using equations (16) and (17), then estimate the instantaneous frequency  $\omega(\tau, f)$  at each time–frequency point via the local time derivative, and finally reassign spectral energy to concentrate oscillatory components:

$$\omega(\tilde{\mathbf{X}}^{\text{STFT}}) = \Re \left( \frac{\partial_{\tau} \tilde{\mathbf{X}}^{\text{STFT}}}{i \tilde{\mathbf{X}}^{\text{STFT}}} \right), \quad (19)$$

where  $i = \sqrt{-1}$  is the imaginary unit, and  $\partial_{\tau} \tilde{\mathbf{X}}^{\text{STFT}}$  is approximated using a central difference operator  $\text{CentralDiff}(\cdot)$ . For a locally mono-component analytic signal  $x(t) = A(t)e^{i\phi(t)}$ , where  $A(t) \geq 0$  and  $\phi(t)$  denote the (slowly-varying) instantaneous amplitude (envelope) and phase, respectively, the STFrFT-based derivation shows that this es-

---

**Algorithm 1:** Fourier-based Synchrosqueezing Transform (FrSST)

---

**Input:** input sequence  $\mathbf{X}$   
**Output:** sharpened time–frequency representation  $\tilde{\mathbf{X}}^{\text{FrSST}}$

- 1  $\tilde{\mathbf{X}}^{\text{STFT}} \leftarrow \text{STFT}(\mathbf{X}, K_f, \frac{K_f}{2}, \text{Hann})$
- 2  $\tilde{\mathbf{X}}^{\text{STFT}} \leftarrow \tilde{\mathbf{X}}^{\text{STFT}} / E_w$ ; // normalize (window)
- 3  $\partial_\tau \tilde{\mathbf{X}}^{\text{STFT}} \leftarrow \text{CentralDiff}(\tilde{\mathbf{X}}^{\text{STFT}})$ ;
- 4  $\omega(\tau, f) \leftarrow \Re\left(\frac{\partial_\tau \tilde{\mathbf{X}}^{\text{STFT}}}{i \cdot \tilde{\mathbf{X}}^{\text{STFT}}}\right)$ ;
- 5  $\xi(\tau, f) \leftarrow \text{Clip}(\text{Round}(\frac{K_f}{2\pi} \cdot \omega(\tau, f)), 0, F - 1)$ ;
- 6  $\tilde{\mathbf{X}}^{\text{FrSST}} \leftarrow \text{ScatterAdd}(\mathbf{0}, \xi, \tilde{\mathbf{X}}^{\text{STFT}})$ ;
- 7 **return**  $\tilde{\mathbf{X}}^{\text{FrSST}}$

---

timator satisfies  $\omega(\tau, f) \approx \phi'(\tau)$ . The estimated frequency is discretized to the nearest bin:

$$\xi(\tilde{\mathbf{X}}^{\text{STFT}}) = \text{Clip}\left(\text{Round}\left(\frac{K_f}{2\pi} \cdot \omega(\tilde{\mathbf{X}}^{\text{STFT}})\right), 0, \frac{K_f}{2}\right), \quad (20)$$

where Clip bounds values to the valid range. Finally, the energy at time  $\tau$  and original frequency  $f$  is reassigned to the estimated bin  $\xi(\tilde{\mathbf{X}}^{\text{STFT}})[\tau, f]$ , forming a sharpened time–frequency representation:

$$\tilde{\mathbf{X}}^{\text{FrSST}} \leftarrow \text{Reassign}(\tilde{\mathbf{X}}^{\text{STFT}}, \xi(\tilde{\mathbf{X}}^{\text{STFT}})). \quad (21)$$

where the Reassign operation denotes this synchrosqueezing-based accumulation. This step enhances the STFT representation by sharpening frequency localization and reducing time–frequency smearing, and is particularly useful for complex non-stationary signals with fast-varying frequency content (e.g., biomedical signals, mechanical vibrations). Algorithm 1 summarizes the complete FrSST procedure.

4) *Computational Complexity:* We briefly summarize the computational cost of the three Fourier-based variants used in the FBP module. Let  $N_{\text{se}}$  denote the total number of univariate series processed in parallel (e.g.,  $N_{\text{se}} = B \times D \times C$ ).

For the DFT-based variant, the 1D real FFT along the temporal axis costs  $\mathcal{O}(T \log T)$ , and the subsequent cosine–sine basis expansion over all frequency–time pairs adds  $\mathcal{O}(FT)$ . Overall, the DFT-based FBP head scales as  $\mathcal{O}(N_{\text{se}}(T \log T + FT))$  in time and  $\mathcal{O}(N_{\text{se}}FT)$  in memory.

For the STFT-based variant, splitting each sequence into  $L$  overlapping frames of length  $K_f$  and applying a  $K_f$ -point FFT to each frame yields time  $\mathcal{O}(LK_f \log K_f)$  and memory  $\mathcal{O}(FL)$  per series. The subsequent modulation and projection in the FBP head are linear in the number of time–frequency coefficients, so the overall complexity is  $\mathcal{O}(N_{\text{se}}(LK_f \log K_f + FL))$  in time and  $\mathcal{O}(N_{\text{se}}FL)$  in memory.

For the FrSST-based variant, we reuse the same STFT representation and perform additional instantaneous-frequency estimation and synchrosqueezing, both of which are linear in the  $F \times L$  coefficients. As a result, the FrSST-based FBP head has the same asymptotic order,  $\mathcal{O}(N_{\text{se}}(LK_f \log K_f + FL))$  in time and  $\mathcal{O}(N_{\text{se}}FL)$  in memory, with a slightly larger constant due to the synchrosqueezing step.

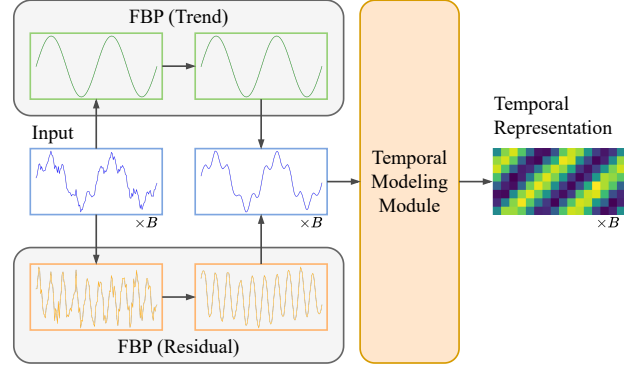


Fig. 3. Architecture of the temporal module. It consists of a FBP block for frequency-enhanced feature extraction, followed by a temporal encoder that models sequential dependencies with attention or gated convolution.

---

**Algorithm 2:** Series Decomposition

---

**Input:** tensor  $\mathbf{X}$ , kernel size  $K_d$   
**Output:** trend component  $\mathbf{X}^{\text{trend}}$ , residual component  $\mathbf{X}^{\text{res}}$

- 1  $W \leftarrow \lfloor \frac{K_d-1}{2} \rfloor$ ;
- 2  $\mathbf{X}^{\text{pad}} \leftarrow \text{PadEdge}(\mathbf{X}, W)$ ;
- 3  $\mathbf{X}^{\text{trend}} \leftarrow \text{AvgPool}(\mathbf{X}^{\text{pad}}, K_d)$ ;
- 4  $\mathbf{X}^{\text{res}} \leftarrow \mathbf{X} - \mathbf{X}^{\text{trend}}$ ;
- 5 **return**  $\mathbf{X}^{\text{trend}}, \mathbf{X}^{\text{res}}$

---

Under our default choice  $K_f = \Theta(T)$  and  $H = K_f/2$ , we have  $L \approx T/H = \Theta(1)$  and  $F = \Theta(K_f)$ , so all three Fourier-based variants exhibit an  $\mathcal{O}(N_{\text{se}}T \log T)$  time complexity with respect to the input length  $T$ , differing only in constant factors and linear terms in  $F$  and  $L$ .

### C. Fourier Bias Projection (FBP)

To introduce explicit frequency modeling and inductive bias into the architecture, we design a temporal module that decomposes the input into trend and residual components and applies FBP to extract frequency-aware features from both branches to guide imputation (Figure 3).

1) *Temporal Decomposition:* We first apply a learnable moving average filter to decompose the input tensor  $\mathbf{X} \in \mathbb{R}^{B \times D \times C \times T}$  into a smooth trend component and a high-frequency residual component:

$$\begin{aligned} \mathbf{X}^{\text{trend}} &= \text{AvgPool1D}(\text{Pad}(\mathbf{X}), K_d), \\ \mathbf{X}^{\text{res}} &= \mathbf{X} - \mathbf{X}^{\text{trend}}. \end{aligned} \quad (22)$$

Here,  $K_d$  controls the temporal smoothing range and is treated as a hyperparameter; the decomposition is summarized in Algorithm 2. After the decomposition, both components are processed by FBP modules instantiated with different Fourier transforms, as detailed in Section IV-B.

2) *Projection onto Fourier Bases:* The architecture of FBP is illustrated in Figure 4. We define fixed orthogonal cosine and sine bases  $\mathbf{b}^{\text{cos}}, \mathbf{b}^{\text{sin}} \in \mathbb{R}^{F \times L}$  as

$$\mathbf{b}^{\text{cos}}[f, \ell] = \cos\left(\frac{2\pi f \ell}{L}\right), \quad \mathbf{b}^{\text{sin}}[f, \ell] = -\sin\left(\frac{2\pi f \ell}{L}\right), \quad (23)$$

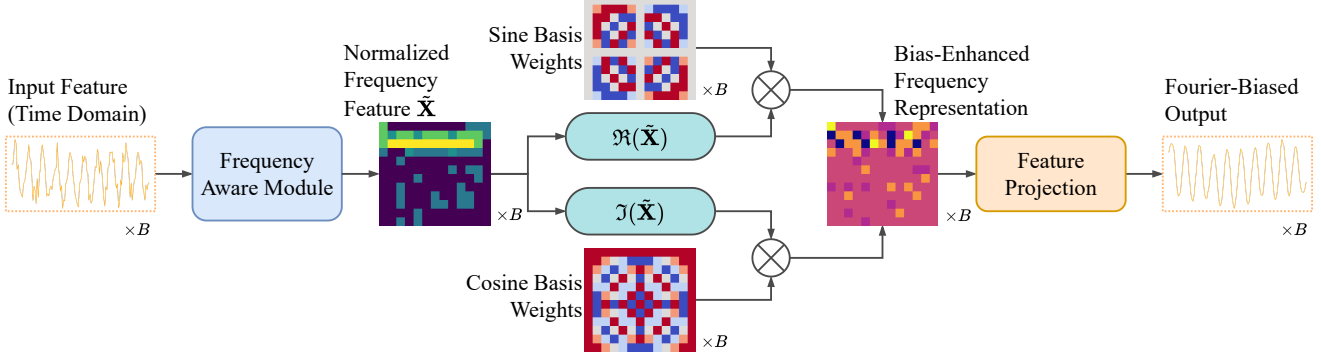


Fig. 4. Structure of the Fourier Bias Projection module. It consists of three operations: (1) a frequency-aware normalization layer that maps input features to spectral space; (2) a bias projection operation that modulates real and imaginary components via learnable sine and cosine bases; and (3) a feature projection layer that produces the final frequency-enhanced representation.

### Algorithm 3: Fourier Bias Projection

---

**Input:** tensor  $\mathbf{X}$ , cosine basis  $\mathbf{b}^{\cos}$ , sine basis  $\mathbf{b}^{\sin}$   
**Output:** frequency-aware features  $\mathbf{X}^{\text{freq}} \in \mathbb{R}^{B \times D \times C \times T}$

- 1  $\tilde{\mathbf{X}} \leftarrow \text{FrequencyAware}(\mathbf{X})$ ;
- 2  $\tilde{\mathbf{X}} \leftarrow \text{Normalization}(\tilde{\mathbf{X}})$ ;
- 3  $\tilde{\mathbf{X}}^{\text{total}} \leftarrow \Re(\tilde{\mathbf{X}}) \cdot \mathbf{b}^{\cos} + \Im(\tilde{\mathbf{X}}) \cdot \mathbf{b}^{\sin}$ ;
- 4  $\mathbf{X}^{\text{freq}} \leftarrow \text{Linear}(\text{Dropout}(\text{Flatten}(\tilde{\mathbf{X}}^{\text{total}})))$ ;
- 5 **return**  $\mathbf{X}^{\text{freq}}$

---

where  $L$  denotes the number of time steps (DFT) or frames (STFT/FrSST). The time–frequency representation is given by:

$$\tilde{\mathbf{X}}^{\text{total}} = \Re(\tilde{\mathbf{X}}) \cdot \mathbf{b}^{\cos} + \Im(\tilde{\mathbf{X}}) \cdot \mathbf{b}^{\sin}, \quad \tilde{\mathbf{X}}^{\text{total}} \in \mathbb{R}^{B \times D \times C \times F \times L}. \quad (24)$$

This projection preserves both magnitude and phase information, allowing the downstream model to access structured time–frequency features. We implement a unified projection interface that supports all three types of spectral transforms, as summarized in Algorithm 3.

In the spectral bias modules, all Fourier-related bases and window functions are fixed and non-trainable, and the DFT/STFT/FrSST operators are used as standard differentiable transforms. The learnable parameters in FBP are restricted to the linear layers that project the spectral representations of the residual and trend components to the target horizon, and gradients are propagated through all spectral operations via autograd for end-to-end training with the temporal backbone.

3) *Motivation and advantages.*: Introducing the frequency-domain bias module brings three main advantages for multivariate time series imputation. First, by constraining the learnable temporal bias to low-frequency Fourier bands, FBP explicitly captures long-term trend and periodic components that are difficult to recover purely in the time domain, especially over long horizons. Second, instead of directly applying a Fourier transform to masked inputs, which yields distorted spectra under severe missingness as shown in Figure 1, FBP learns the bias within the conditional diffusion process and then projects it into the spectral domain, leading to more stable and faithful frequency representations. Third, the

low-frequency parameterization provides structural inductive bias (smoothness and periodicity) and spectral regularization, improving robustness and generalization under scarce or distribution-shifted data, while remaining compatible with different Fourier transforms within our framework.

### D. Temporal Modeling Module

To model temporal dependencies during denoising, we design a temporal module that integrates frequency-aware signals from FBP with self-attention or temporal convolution. As illustrated in Figure 3, the projected frequency features are fused with the input sequence and then fed into stacked attention or convolution blocks. Concretely, we use the output of FBP (Algorithm 3) as the input to the temporal module, denoted by  $\mathbf{V} \triangleq \mathbf{X}^{\text{freq}}$ . This design enables flexible modeling of both global frequency structures and local temporal patterns.

1) *Self-Attention for Temporal Modeling*: To model complex temporal dependencies, we employ self-attention mechanisms based on the Transformer architecture [45]. The encoder consists of stacked attention layers with residual connections, feedforward networks, and layer normalization. We use standard scaled dot-product multi-head self-attention [45], where each layer operates on a query–key–value triplet  $(\mathbf{Q}, \mathbf{K}, \mathbf{V})$  and aggregates information along the temporal dimension. We denote the output of the  $L$ -th self-attention layer by

$$\mathbf{V}^{\text{out}} = \text{Transformer}(\mathbf{Q}, \mathbf{K}, \mathbf{V}). \quad (25)$$

In the temporal configuration, each variable is treated as a sequence along time, so the inputs are reshaped to  $(B \times D, C, T)$  and self-attention is applied to capture temporal dependencies.

2) *Temporal Convolution*: To complement self-attention, we incorporate a gated temporal convolutional network (TCN) inspired by WaveNet [41]. In the temporal configuration, each variable is treated as a sequence along time, so the inputs are reshaped to  $(B \times D, C, T)$ , and TCN is applied to capture long-range temporal dependencies. Our temporal convolution module is implemented as a stacked gated dilated convolutional network composed of multiple blocks and layers with exponentially increasing dilation rates, and it processes inputs  $\mathbf{V} \in \mathbb{R}^{B \times D \times C \times T}$ . Each layer applies two parallel dilated

convolutions with the same dilation but different weights: one uses a tanh nonlinearity to produce the filter activation, and the other uses a sigmoid function to produce the gate. The outputs are combined element-wise:

$$\mathbf{Y} = \tanh(\text{Conv}_{\text{filter}}(\mathbf{V})) \odot \sigma(\text{Conv}_{\text{gate}}(\mathbf{V})), \quad (26)$$

where  $\odot$  denotes element-wise multiplication. Each gated layer produces both a residual output and a skip connection. The residual is added back to the input after a  $1 \times 1$  convolution and batch normalization:

$$\mathbf{V}^{\text{res}} = \text{BatchNorm}(\mathbf{V} + \text{Conv}(\mathbf{Y})), \quad (27)$$

and the skip path collects outputs from all layers:

$$\mathbf{S}^{\text{total}} = \sum_{i=1}^L \text{Conv}^{(i)}(\mathbf{Y}^{(i)}). \quad (28)$$

The aggregated skip output is passed through two projection layers with ReLU activation to produce the final output:

$$\mathbf{V}^{\text{out}} = \text{Conv}_{\text{final}}(\text{ReLU}(\text{Conv}_{\text{inter}}(\text{ReLU}(\mathbf{S}^{\text{total}}))))). \quad (29)$$

The resulting tensor  $\mathbf{V}^{\text{out}}$  is used for downstream modeling or fused with outputs from other modules such as attention layers. This TCN module can replace temporal self-attention, providing a fixed receptive field and improved parameter efficiency for localized dynamics.

#### E. Feature Attention Module

We apply self-attention along the feature dimension to model cross-variable dependencies. We reuse the temporal self-attention encoder from Sec. IV-D1, but apply it along the feature axis instead of the temporal axis. At each time step, the  $D$  variables are treated as a feature vector, and self-attention operates across features. The input is reshaped accordingly so that the attention operates on sequences of length  $D$ , with inputs of shape  $(B \times T, C, D)$ . Sharing the same encoder structure allows us to reuse the core logic with different input shapes and semantics depending on whether we model time or features. This design enables flexible, modular integration of attention into different components of the diffusion process.

#### F. Training

We train the diffusion model for conditional time series imputation using a denoising score matching objective that minimizes the discrepancy between the injected noise and the predicted noise on masked regions.

At each iteration, given an input time series  $\mathbf{X} \in \mathbb{R}^{B \times T \times D}$  and its observation mask  $\mathbf{M} \in \{0, 1\}^{B \times T \times D}$ , we sample an auxiliary mask for corruption. A random binary mask  $\mathbf{M}^{\text{co}} \in \{0, 1\}^{B \times T \times D}$  is sampled from the observation mask  $\mathbf{M}$  to simulate additional missing entries during training. This element-wise sampling produces a mixture of isolated missing points and short contiguous gaps across variables, rather than enforcing a specific missing pattern. The model is then trained to impute the difference  $\mathbf{M}^{\text{ta}} = \mathbf{M} - \mathbf{M}^{\text{co}}$ , which identifies entries that were originally observed but are intentionally masked during training for supervision.

1) *Noise Corruption and Denoising*: At each iteration, we sample  $s \sim \mathcal{U}(1, S)$  and extend the forward diffusion in Eq. (4) to the tensor  $\mathbf{X}$  to obtain a noisy tensor  $\mathbf{X}_s$ :

$$\begin{aligned} \mathbf{X}_s &= \sqrt{\bar{\alpha}_s} \mathbf{X} + \sqrt{1 - \bar{\alpha}_s} \boldsymbol{\epsilon}, \quad \boldsymbol{\epsilon} \sim \mathcal{N}(0, \mathbf{I}), \\ \mathbf{X}_s^{\text{ta}} &= \text{Concat}(\mathbf{M}^{\text{co}} \odot \mathbf{X}, (1 - \mathbf{M}^{\text{co}}) \odot \mathbf{X}_s). \end{aligned} \quad (30)$$

Here,  $\bar{\alpha}_s$  denotes the cumulative noise schedule that controls the signal-to-noise ratio at step  $s$ , and  $\boldsymbol{\epsilon}$  is the standard Gaussian noise added to simulate corruption, which is the most common choice in DDPM-based models; alternative noise distributions (Laplace and uniform) are further evaluated in our ablation study. Here,  $\bar{\alpha}_s$  is the cumulative noise schedule that controls the signal-to-noise ratio at step  $s$ , and  $\boldsymbol{\epsilon}$  is standard Gaussian noise, following the common choice in DDPM-based models. In all experiments we fix the number of diffusion steps to  $S = 50$  and use a quadratic variance schedule  $\{\beta_s\}_{s=1}^S$  between  $\beta_{\text{start}} = 10^{-4}$  and  $\beta_{\text{end}} = 0.5$ , with  $\alpha_s = 1 - \beta_s$  and  $\bar{\alpha}_s = \prod_{i=1}^s \alpha_i$ . We then feed the masked-and-noisy input together with the diffusion step and conditional features into the denoising network, yielding the noise prediction  $\hat{\boldsymbol{\epsilon}} = \epsilon_{\theta}(\mathbf{X}_s^{\text{ta}}, s, \mathbf{X}^{\text{cf}})$ .

2) *Loss Function*: We follow the  $\varepsilon$ -parameterization of DDPM and adapt the standard objective in Eq. (8) by restricting it to masked entries:

$$\mathcal{L}_{\text{train}} = \frac{1}{|\mathbf{M}^{\text{ta}}|} \|(\boldsymbol{\epsilon} - \hat{\boldsymbol{\epsilon}}) \odot \mathbf{M}^{\text{ta}}\|_2^2. \quad (31)$$

During training we sample one diffusion step  $s$  per batch and compute the loss at that step. During validation, we compute the average denoising loss across all diffusion steps.

3) *Side Information*: We further inject side information (e.g., time and variable embeddings) extracted from timestamps and the observation mask into the denoising model. This helps the model identify missing positions and provides positional awareness for irregularly sampled time series.

#### G. Sampling Strategy during Inference

At inference time, we perform imputation by sampling from the learned reverse diffusion process, starting from Gaussian noise on the missing regions and iteratively denoising the sequence. Our sampling strategy consists of three stages: initialization, conditional reverse sampling, and multiple-sample aggregation, and uses the standard ancestral DDPM sampler with the same noise schedule and  $S = 50$  steps, without classifier-based or classifier-free guidance.

1) *Initialization*: Given an observed time series  $\mathbf{X}$  and a binary mask  $\mathbf{M}^{\text{co}}$  indicating observed positions, we keep the conditional part fixed as  $\mathbf{X}^{\text{co}} = \mathbf{M}^{\text{co}} \odot \mathbf{X}$  and initialize the target part with Gaussian noise  $\mathbf{X}_S^{\text{ta}} \sim \mathcal{N}(0, \mathbf{I})$ .

2) *Conditional Reverse Sampling*: Starting from  $s = S$ , we iteratively update the sample via the reverse diffusion equation. At each step  $s$ , we form the model input by combining the fixed conditional observations with the current target sample:

$$\mathbf{X}_s^{\text{ta}} = \text{Concat}(\mathbf{X}^{\text{co}}, (1 - \mathbf{M}^{\text{co}}) \odot \mathbf{X}_s^{\text{ta}}). \quad (32)$$

We then obtain the noise prediction  $\hat{\epsilon}_s = \epsilon_\theta(\mathbf{X}_s^{\text{ta}}, s, \mathbf{X}^{\text{cf}})$  and update the sample at the previous diffusion step  $s-1$  as

$$\mathbf{X}_{s-1}^{\text{ta}} = \frac{1}{\sqrt{\bar{\alpha}_s}} \left( \mathbf{X}_s^{\text{ta}} - \frac{1 - \bar{\alpha}_s}{\sqrt{1 - \alpha_s}} \hat{\epsilon}_s \right) + \sigma_s \zeta, \quad \zeta \sim \mathcal{N}(0, \mathbf{I}), \quad (33)$$

where  $\bar{\alpha}_s$  is the cumulative noise schedule and  $\sigma_s$  is the posterior noise scale.

3) *Multiple Sampling*: To improve robustness, we generate  $K$  imputation samples by repeating the reverse process and average them:

$$\hat{\mathbf{X}} = \frac{1}{K} \sum_{k=1}^K (\mathbf{X}_0^{\text{ta}})_k, \quad (34)$$

where each  $(\mathbf{X}_0^{\text{ta}})_k$  is an independent diffusion trajectory starting from a different Gaussian initialization.

## V. EXPERIMENTS

We conduct experiments to evaluate the effectiveness, efficiency, and robustness of our model for multivariate time series imputation, covering different missing patterns and rates, uncertainty estimation, sampling efficiency, and ablations on frequency and temporal modules.

### A. Experimental Setup

1) *Datasets*: We evaluate our model on four real-world multivariate time series datasets from diverse domains: ETT [67], Weather [10], METR-LA [68], and Yeast [69]. ETT contains transformer temperature and load readings, Weather consists of meteorological variables such as temperature and humidity, and METR-LA captures traffic speed measurements from loop detectors in Los Angeles; for METR-LA we consider both full (207 sensors) and reduced (9 sensors) feature settings in case studies.

The Yeast dataset originates from single-cell biological experiments, where cell morphology and gene expression are tracked over time. Among several available subsets, we use Set2, which contains 3456 cell trajectories with 185 time steps each. From the original 12 variables, we select 7 continuous features describing cell shape and size (length, width, area, perimeter), fluorescence intensity (flu01), image sharpness (sharpness), and cell count (cell\_count). We discard chamber-level aggregates (e.g., chamber\_mean\_flu01), which obscure single-cell dynamics, and binary intervention indicators (e.g., stims), which encode external perturbations and are not continuous imputation targets. To the best of our knowledge, this is the first work to incorporate the Yeast dataset into a time series imputation benchmark, highlighting its potential for evaluating robustness in noisy, non-periodic biological dynamics. A summary of dataset characteristics is provided in Table II. Each dataset is normalized before training, and the input features are masked according to the missing settings described below.

2) *Missing Settings*: To simulate realistic missing scenarios, we consider two common patterns:

- **Point-wise missing**: individual values are randomly masked across time and features.

TABLE II  
SUMMARY OF DATASETS USED IN THE EXPERIMENTS.

Dataset	Domain	Feat.	Steps	Interval	Miss (%)
ETTm1	Energy	7	96	15 min	0
Weather	Meteo.	21	144	10 min	0.02
METR-LA	Traffic	207(9)	288	5 min	8.6
Yeast	Biology	7	185	5 min	0

- **Time-wise missing**: continuous blocks of time steps are masked for each feature, simulating sensor downtime or communication failures.

We evaluate each model under 10% and 50% missing rates. The same missing masks are applied across all methods for fair comparison.

3) *Evaluation Metrics*: We assess imputation performance using four metrics:

- **MAE** (Mean Absolute Error): average absolute deviation between imputed and ground truth values [70].
- **MRSE** (Mean Relative Squared Error): squared error normalized by the variance of the ground truth [10], [19].
- **MAPE** (Mean Absolute Percentage Error): captures relative errors and is particularly informative when values span different scales [70], [71].
- **CRPS** (Continuous Ranked Probability Score): measures both calibration and sharpness of the predictive distribution for probabilistic models [72].

4) *Baselines*: We compare our method against the following baselines:

- **Traditional Statistical Methods**: Mean and Median imputation fill missing values with global statistics.
- **Classical Learning-based Models**: KNN leverages distance-based similarity between samples; BRITS [37] uses bidirectional RNNs to capture sequential dependencies during imputation.
- **Transformer-based Models**: SAITS [10] applies structured self-attention for imputation; TimesNet [14] exploits temporal blocks with frequency-aware modules; TimeMixer [73] uses token-mixing MLPs on decomposed seasonal and trend components, and TimeMixer++ [74] extends it with multi-resolution temporal representations.
- **Diffusion-based Models**: CSDI [19] introduces conditional score-based diffusion for flexible probabilistic imputation; MTSCI [20] improves temporal coherence via consistency constraints implemented with contrastive masking and conditional mixup.

Notably, both TimesNet and TimeMixer++ leverage **frequency domain modeling** (e.g., via Fourier transform), which is also a key component of our architecture. This allows for a fair comparison of frequency-aware imputation strategies.

All models are implemented in PyTorch and trained on a single NVIDIA RTX A5000 GPU. We use the same optimizer settings and batch sizes for all methods, and report results averaged over five random seeds with different missing masks.

### B. Imputation Accuracy under Different Missing Patterns

Table III reports MAE results under both point-wise and time-wise missing patterns. Our model attains the lowest MAE in most settings and remains within the top three across all datasets and missing rates. Throughout the result tables, gray cells denote the top three methods and **bold** denotes the best; “–” marks models that cannot be applied to Yeast, such as TimeMixer and TimeMixer++, whose architectural assumptions cannot handle the irregular sequence length  $T = 185$ .

1) *Point-wise Missing Patterns*: Under point-wise missing, our model achieves the best MAE in 5 out of 6 settings and ranks third only on Weather at a 10% missing rate. We also observe that the relative gains of our method tend to increase at the higher missing rate (0.5), especially on Weather and Yeast, suggesting that the combination of diffusion-based modeling with frequency-aware reconstruction is particularly beneficial under severe data sparsity.

2) *Time-wise Missing Patterns*: Under time-wise missing, our model attains the lowest MAE in 5 out of 6 settings; the only exception is Yeast at a 50% missing rate, where it trails MTSCI by just 0.04. Compared with the point-wise setting, SAITS and diffusion-based models such as CSDI and MTSCI suffer substantial performance drops under time-wise missing, especially on Weather and Yeast. This suggests that the absence of explicit frequency modeling makes it harder to recover structured temporal gaps, and highlights the benefit of our frequency-aware design. Within the time-wise setting, methods with stronger temporal modeling, such as TimesNet and BRITS, tend to outperform models without explicit temporal mechanisms, underscoring the importance of temporal-dependency modeling for long gaps; our model, combining frequency-domain bias with a strong temporal backbone, remains among the top performers across all datasets.

### C. Robustness and Uncertainty Evaluation

In addition to MAE, we evaluate our model with metrics that capture uncertainty quality, robustness to extreme errors, and relative accuracy across scales. For clarity, we report these metrics only for learning-based baselines and our method, omitting simple imputers (mean, median, KNN) whose removal does not change any comparative conclusion.

1) *Uncertainty Modeling*: To assess how well models capture uncertainty in the imputation process, we use CRPS, which evaluates the accuracy of the predicted distribution (lower is better) rather than just point estimates. Table IV reports the CRPS scores under varying missing patterns and datasets. Our model achieves the lowest CRPS in most cases and is consistently among the top three elsewhere, indicating substantially better calibrated and sharper predictive distributions than existing baselines on these benchmarks. Our model achieves the lowest CRPS in most cases and is always among the top three, indicating that it produces accurate and sharp probabilistic imputations across datasets and missing patterns.

2) *Robustness to Extreme Errors*: We evaluate robustness using RMSE, which penalizes large deviations more heavily than MAE due to its quadratic formulation. As shown in Table V, our model is among the top three methods in 10

out of 12 dataset–pattern combinations, and often achieves the best RMSE. This shows that FADTI remains competitive when large local errors have a stronger impact on the evaluation.

3) *Relative Error across Scales*: Absolute error metrics such as MAE and RMSE do not reflect the relative scale of errors across features with different magnitudes, so we also report MAPE as a complementary metric. As shown in Table VI, FADTI ranks within the top three methods in most dataset–pattern combinations and often achieves the best MAPE, suggesting that, on these benchmarks, it preserves the relative scale of the original time series more faithfully than competing approaches.

### D. Ablation Study: Frequency and Temporal Modules

To evaluate the contributions of the frequency and temporal modeling components, we perform an ablation study over eight model variants obtained by combining four frequency modules (None, DFT, STFT, FrSST) with two temporal backbones (Attention and Convolution). This setup allows us to assess how inductive biases from frequency-domain representations affect the model’s generalization and robustness.

As shown in Table VII, variants without a frequency module (None-Attn/None-Conv) consistently give the worst MAE in each dataset–pattern–rate setting, indicating that frequency-domain information is critical for accurate imputation. We mark the worst-performing variant in each setting with red. Across all dataset–pattern–rate combinations in Table VII, the best-performing variant always uses one of the Fourier modules (DFT, STFT, or FrSST), whereas the worst MAE almost always comes from a model without frequency modeling (None-Attn or None-Conv). This shows that FBP is the main driver of the performance gains and that frequency-domain information is crucial for accurate imputation. Among Fourier-equipped models, DFT-based variants, especially DFT-Attn, are strongest on long-sequence datasets such as ETT and Weather, while STFT-Conv and, at higher missing rates, FrSST-based variants are more competitive under time-wise missing patterns, suggesting that localized and finer frequency representations help under contiguous gaps and sparse observations. Both attention and gated convolutions thus serve as effective temporal backbones, with their relative advantage modest and dataset- and pattern-dependent compared with the impact of the Fourier module.

### E. Comparison with Diffusion-based Baselines

To compare FADTI with other diffusion-based imputers, we vary the number of reverse-diffusion steps ( $n_{\text{sample}}$ ) and analyze their impact on accuracy and efficiency.

1) *Stability and Efficiency on ETT Dataset*: As shown in Figure 5, we plot MAE and CRPS against inference time on the ETT dataset, using the same sampling schedule with  $n_{\text{sample}}$  ranging from 2 to 28 for all models. For fairness, we retrain all methods under identical experimental configurations, including the missing patterns, missing ratios, and train/validation/test splits.

While increasing  $n_{\text{sample}}$  generally lowers the error at the cost of longer inference time, the marginal improvement in

TABLE III

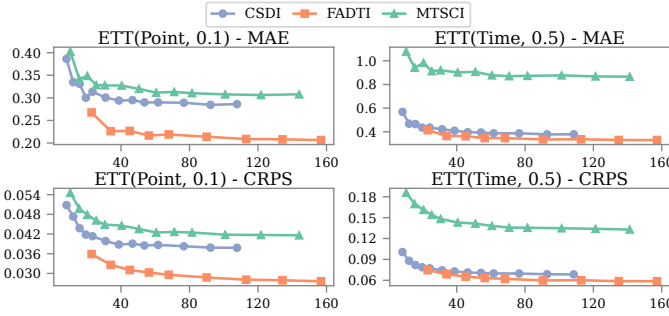
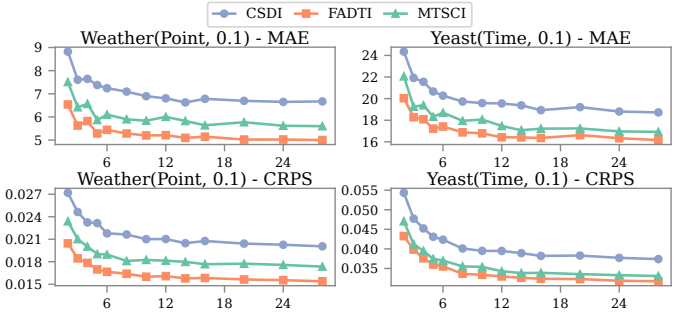
MAE ( $\downarrow$ ) OF DIFFERENT IMPUTATION METHODS UNDER POINT- AND TIME-WISE MISSING PATTERNS ON THE ETT, WEATHER, AND YEAST DATASETS.

Method	ETT				Weather				Yeast			
	Point		Time		Point		Time		Point		Time	
	0.1	0.5	0.1	0.5	0.1	0.5	0.1	0.5	0.1	0.5	0.1	0.5
Mean	2.485	2.487	2.477	2.483	81.890	81.145	81.166	81.173	190.875	191.444	190.532	191.120
Median	2.399	2.401	2.383	2.395	68.883	68.269	68.224	68.030	168.183	169.279	168.607	168.661
KNN	1.037	1.445	1.450	1.501	23.428	28.084	24.663	27.358	137.771	144.068	137.051	141.542
BRITS	0.317	0.558	0.505	0.758	9.119	12.416	12.262	16.976	20.388	31.619	24.176	46.691
SAITS	0.939	1.239	2.199	2.182	30.231	70.782	156.038	149.107	63.263	78.286	299.771	361.723
TimesNet	0.599	0.553	0.593	0.562	13.435	12.935	13.578	12.997	17.038	18.939	21.429	28.751
TimeMixer	2.358	2.331	2.344	2.346	114.180	116.147	117.844	116.006	—	—	—	—
TimeMixer++	1.026	0.951	1.234	1.168	50.108	74.575	30.214	29.760	—	—	—	—
CSDI	0.240	0.327	0.452	0.617	6.347	9.184	41.433	41.443	7.013	10.876	20.138	21.546
MTSCI	0.248	0.332	0.844	0.722	5.574	8.199	41.568	41.165	7.392	10.238	17.580	19.449
FADTI	<b>0.197</b>	<b>0.283</b>	<b>0.329</b>	<b>0.377</b>	6.946	<b>6.327</b>	<b>9.279</b>	<b>8.271</b>	<b>5.950</b>	<b>9.438</b>	<b>16.987</b>	19.493

TABLE IV

CRPS ( $\downarrow$ ) OF DIFFERENT IMPUTATION METHODS UNDER POINT- AND TIME-WISE MISSING PATTERNS ON THE ETT, WEATHER, AND YEAST DATASETS.

Method	ETT				Weather				Yeast			
	Point		Time		Point		Time		Point		Time	
	0.1	0.5	0.1	0.5	0.1	0.5	0.1	0.5	0.1	0.5	0.1	0.5
BRITS	0.066	0.118	0.107	0.160	0.036	0.049	0.049	0.068	0.053	0.084	0.064	0.122
SAITS	0.200	0.258	0.471	0.475	0.113	0.263	0.571	0.546	0.155	0.192	0.748	0.910
TimesNet	0.122	0.114	0.122	0.116	0.052	0.050	0.053	0.051	0.044	0.052	0.055	0.077
TimeMixer	0.494	0.492	0.495	0.496	0.444	0.454	0.459	0.452	—	—	—	—
TimeMixer++	0.213	0.200	0.264	0.241	0.193	0.301	0.119	0.117	—	—	—	—
CSDI	0.039	0.053	0.077	0.100	0.020	0.029	0.133	0.132	0.015	0.022	0.041	0.044
MTSCI	0.040	0.054	0.125	0.113	0.018	0.026	0.155	0.153	0.015	0.021	0.035	<b>0.039</b>
FADTI	<b>0.032</b>	<b>0.046</b>	<b>0.054</b>	<b>0.062</b>	0.021	<b>0.020</b>	<b>0.029</b>	<b>0.025</b>	<b>0.012</b>	<b>0.019</b>	<b>0.034</b>	0.039

Fig. 5. MAE and CRPS of FADTI, CSDI, and MTSCI on the ETT dataset for different diffusion sample sizes ( $n_{\text{sample}}$ ). The x-axis shows inference time (seconds), and the y-axis shows the value of the metric displayed in each panel.Fig. 6. MAE and CRPS of FADTI, CSDI, and MTSCI versus diffusion sample size ( $n_{\text{sample}}$ ) on the Weather and Yeast datasets. The x-axis shows  $n_{\text{sample}}$ , and the y-axis shows the value of the metric displayed in each panel.

metrics (e.g., MAE) becomes negligible after  $n_{\text{sample}} = 20$ . Across all sampling budgets on ETT, FADTI achieves the best MAE and CRPS. Under the missing rate of 0.1, it already outperforms other diffusion-based methods with very few samples; for example, FADTI with  $n_{\text{sample}} = 2$  attains lower MAE and CRPS than competing models with  $n_{\text{sample}} = 28$ . This indicates that FADTI is not only more accurate but also more sample-efficient, reaching its performance plateau with

far fewer diffusion steps.

2) *Cross-dataset Superiority*: In Figure 6, we further compare FADTI with diffusion-based baselines on two datasets: Weather and Yeast. We report MAE and CRPS as complementary metrics: MAE reflects point-wise reconstruction accuracy, whereas CRPS evaluates the quality of the predictive distribution, combining calibration and sharpness.

Across the two datasets and the range of sampling steps

TABLE V

RMSE ( $\downarrow$ ) OF DIFFERENT IMPUTATION METHODS UNDER POINT- AND TIME-WISE MISSING PATTERNS ON THE ETT, WEATHER, AND YEAST DATASETS.

Method	ETT				Weather				Yeast			
	Point		Time		Point		Time		Point		Time	
	0.1	0.5	0.1	0.5	0.1	0.5	0.1	0.5	0.1	0.5	0.1	0.5
BRITS	0.611	0.965	0.914	1.300	98.494	98.511	97.142	98.085	88.061	106.228	92.673	129.701
SAITS	1.233	1.762	2.957	2.830	84.787	125.580	281.806	281.272	104.120	131.307	607.420	765.427
TimesNet	1.087	0.966	1.049	0.986	98.492	92.576	99.691	92.487	55.631	58.444	70.217	84.853
TimeMixer	3.276	3.236	3.248	3.251	180.488	179.092	175.149	173.087	—	—	—	—
TimeMixer++	1.809	1.734	2.197	2.030	146.172	162.833	109.739	109.648	—	—	—	—
CSDI	0.415	0.619	0.845	1.081	92.844	95.956	134.245	129.377	37.297	56.051	97.569	97.213
MTSCI	0.422	0.631	1.350	1.248	93.834	91.810	134.011	127.124	37.946	53.769	90.929	95.317
FADTI	0.329	0.636	0.656	0.744	165.712	93.906	142.726	89.942	34.580	52.556	89.012	93.621

TABLE VI

MAPE ( $\downarrow$ ) OF DIFFERENT IMPUTATION METHODS UNDER POINT- AND TIME-WISE MISSING PATTERNS ON THE ETT, WEATHER, AND YEAST DATASETS.

Method	ETT				Weather				Yeast			
	Point		Time		Point		Time		Point		Time	
	0.1	0.5	0.1	0.5	0.1	0.5	0.1	0.5	0.1	0.5	0.1	0.5
BRITS	2.753	4.943	5.429	13.053	47.646	58.985	56.548	98.830	118.417	257.319	134.756	315.851
SAITS	9.364	13.130	10.979	13.059	70.991	145.772	372.039	322.303	2339.250	545.734	1174.880	1431.712
TimesNet	6.163	5.753	5.792	8.746	83.147	75.549	160.780	83.892	538.301	140.514	88.964	167.337
TimeMixer	3.147	3.140	3.286	3.266	178.898	165.654	171.114	172.899	—	—	—	—
TimeMixer++	7.026	8.369	13.110	18.127	404.689	240.239	373.255	226.294	—	—	—	—
CSDI	4.120	3.641	5.061	15.368	58.883	67.633	127.624	144.451	42.377	103.915	105.940	162.367
MTSCI	3.138	3.501	8.116	19.140	47.520	55.445	164.446	124.210	38.238	101.122	100.902	137.851
FADTI	3.132	2.657	4.087	9.737	55.496	48.685	67.157	81.335	42.741	102.484	98.850	146.718

considered, FADTI attains the lowest MAE and CRPS in all settings, yielding consistent gains over existing diffusion-based imputers. This indicates that our model is effective across diverse temporal dynamics and missing patterns, and remains robust as the sampling budget varies.

#### F. Case Study: Long-Range Robustness on METR-LA

To better understand the behavior of our model under different temporal horizons, we conduct a case study on the METR-LA dataset using two evaluation configurations: (1) all 207 sensors with a 24-step horizon; and (2) 9 sensors with the full 288-step horizon. Figure 7 presents the performance comparison under the point-wise missing pattern with a 10% missing rate, evaluated across four metrics: MAE, RMSE, CRPS, and MAPE. Each subfigure compares model performance across the two settings and also includes the performance difference between the long- and short-horizon configurations. Specifically, for each method and metric we compute the absolute performance difference ( $\Delta = \text{Score}_{T=288} - \text{Score}_{T=24}$ ) to highlight sensitivity to sequence length.

Across all four metrics, FADTI exhibits a markedly smaller performance drop when moving from the short to the long horizon than competing methods, suggesting stronger long-term temporal modeling. This case study indicates that FADTI remains robust in long-range imputation settings.

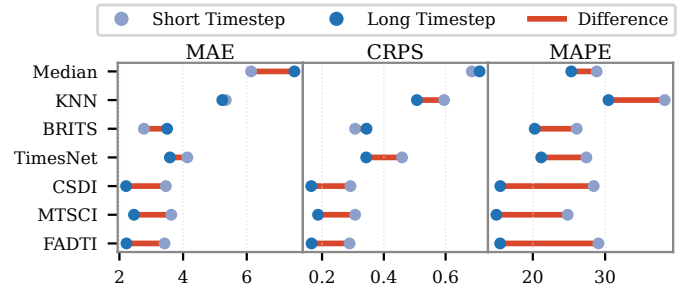


Fig. 7. Performance comparison on the METR-LA dataset (point-wise, 10% missing). Each subfigure shows MAE, CRPS, and MAPE under short and long timestep settings, with red line segments indicating the performance gaps ( $\Delta$ ) between them.

#### G. Sensitivity to Noise Distributions

We evaluate the impact of different corruption distributions in the forward diffusion process by replacing the standard Gaussian noise with Laplace and Uniform variants. Figure 8 summarizes the relative error across metrics. Gaussian noise consistently yields the best performance on both datasets, while Laplace produces only minor degradation. In contrast, Uniform noise leads to substantial failure, with errors increasing by orders of magnitude.

These results indicate that diffusion-based time-series imputers are sensitive to the choice of noise distribution, and

TABLE VII

MAE ( $\downarrow$ ) OF ABLATED FADTI VARIANTS ON ETT, WEATHER, AND METR\_LA WITH POINT-WISE AND TIME-WISE MISSING RATES OF 0.1 AND 0.5. EACH VARIANT COMBINES ONE OF FOUR FREQUENCY MODULES (NONE, DFT, STFT, FRSSST) WITH ATTENTION OR CONVOLUTION.

Method	ETT				Weather				Metr_LA			
	Point		Time		Point		Time		Point		Time	
	0.1	0.5	0.1	0.5	0.1	0.5	0.1	0.5	0.1	0.5	0.1	0.5
None-Attn	0.296	0.296	1.165	0.558	5.926	8.591	40.842	39.812	3.440	3.625	4.101	4.637
None-Conv	0.287	0.479	0.428	0.633	6.253	7.446	9.840	11.462	3.599	3.801	3.818	4.413
FrSST-Attn	0.287	0.401	0.307	0.318	6.111	7.211	9.865	9.647	3.439	3.609	4.280	4.456
FrSST-Conv	0.275	0.339	0.361	0.386	5.753	6.996	8.367	9.160	3.510	3.723	3.664	4.228
STFT-Attn	0.204	0.277	0.300	0.321	5.338	6.642	7.818	9.807	3.414	3.649	3.783	4.374
STFT-Conv	0.205	0.269	0.298	0.341	5.004	6.895	6.882	7.671	3.487	3.677	3.526	4.093
DFT-Attn	<b>0.193</b>	<b>0.221</b>	0.332	0.320	<b>4.182</b>	<b>5.804</b>	7.422	<b>7.345</b>	3.414	3.714	3.898	4.292
DFT-Conv	0.198	0.255	<b>0.246</b>	<b>0.316</b>	5.560	5.866	11.234	8.191	<b>3.394</b>	3.738	3.701	<b>4.039</b>

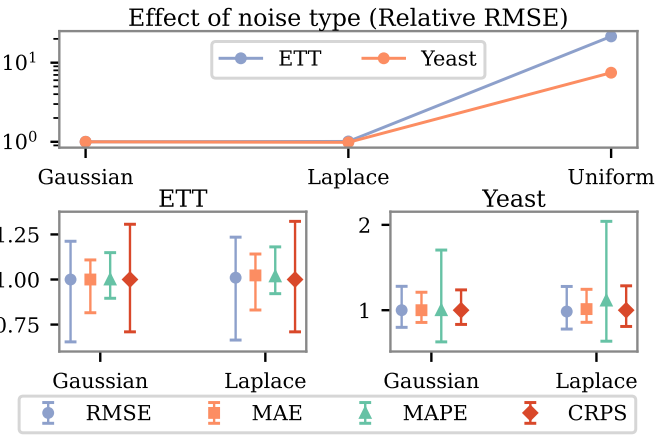


Fig. 8. Noise sensitivity analysis. (a) RMSE under Gaussian, Laplace, and Uniform noise (normalized to the Gaussian case); Uniform severely degrades performance. (b-c) Relative RMSE/MAE/MAPE/CRPS under Gaussian vs Laplace on ETT and Yeast, with min-max error bars.

Gaussian noise aligns best with the underlying diffusion dynamics. Its smooth, isotropic perturbations preserve local temporal structure and yield stable score estimates, whereas heavy-tailed (Laplace) or non-smooth (Uniform) perturbations distort trajectories and hinder the reverse denoising process.

#### H. Limitations and Future Work

Despite its strong performance across diverse benchmarks, FADTI has several limitations. First, the method is more computationally expensive than deterministic imputers such as SAITS or BRITS, since each prediction requires multiple diffusion steps and an extra spectral projection module; this improves uncertainty estimation but increases training and inference time, which may be unsuitable for real-time applications. Second, the approach relies on frequency-based inductive biases that assume smooth trends or quasi-periodic structure, so its advantage may shrink on highly irregular, event-driven series where simpler architectures remain competitive. From a scalability perspective, our experiments only cover multivariate series with up to  $D = 207$  variables (METR\_LA), and we have not systematically evaluated very long horizons or regimes with thousands of variables. Extending the framework

to higher-dimensional regimes, heavily irregular sampling, and non-Gaussian observation noise is left for future work.

## VI. CONCLUSION

We proposed FADTI, a conditional diffusion framework for multivariate time series imputation that combines frequency-informed modulation with feature-wise temporal modeling. To address uncertainty handling and lack of frequency-domain inductive biases in existing methods, we introduced the FBP module, which flexibly incorporates Fourier-based transforms rooted in classical signal processing, including DFT, STFT, and FrSST. We instantiate FBP with all three transforms and, to the best of our knowledge, apply STFT and FrSST to multivariate time series imputation for the first time.

Extensive experiments show that FADTI achieves state-of-the-art performance across diverse datasets and missing patterns, with particularly strong gains at high missing rates. Ablation studies further confirm the importance of frequency-domain priors, implemented via FBP, for improving imputation accuracy. Future work includes extensions to irregular time grids, adaptive spectral transforms, and downstream tasks such as forecasting and anomaly detection.

## REFERENCES

- [1] Z. Che, S. Purushotham, K. Cho, D. A. Sontag, and Y. Liu, “Recurrent neural networks for multivariate time series with missing values,” *Sci. Rep.*, vol. 8, no. 1, p. 6085, 2018.
- [2] Y. Kim and M. Chi, “Temporal belief memory: Imputing missing data during RNN training,” in *Proc. Int. Joint Conf. Artif. Intell. (IJCAI)*, 2018, pp. 2326–2332.
- [3] I. Silva, G. Moody, D. J. Scott, L. A. Celi, and R. G. Mark, “Predicting in-hospital mortality of icu patients: The physionet/computing in cardiology challenge 2012,” in *Comput. Cardiol. Conf. (CinC)*, 2012, pp. 245–248.
- [4] J. Bai and S. Ng, “Forecasting economic time series using targeted predictors,” *J. Econometrics*, vol. 146, no. 2, pp. 304–317, 2008.
- [5] X. Li, H. Li, H. K. Chan, H. Lu, and C. S. Jensen, “Data imputation for sparse radio maps in indoor positioning,” in *IEEE Int. Conf. Data Eng. (ICDE)*, 2023, pp. 2235–2248.
- [6] Y. Gong, Z. Li, J. Zhang, W. Liu, Y. Yin, and Y. Zheng, “Missing value imputation for multi-view urban statistical data via spatial correlation learning,” *IEEE Trans. Knowl. Data Eng.*, vol. 35, no. 1, pp. 686–698, 2023.
- [7] J. G. Ibrahim, H. Chu, and M.-H. Chen, “Missing data in clinical studies: issues and methods,” *J. Clin. Oncol.*, vol. 30, no. 26, pp. 3297–3303, 2012.

[8] C. Esteban, S. L. Hyland, and G. Rätsch, “Real-valued (medical) time series generation with recurrent conditional gans,” *CoRR*, vol. abs/1706.02633, 2017.

[9] L. Qian, T. Wang, J. Wang, H. L. Ellis, R. Mitra, R. J. B. Dobson, and Z. M. Ibrahim, “How deep is your guess? A fresh perspective on deep learning for medical time-series imputation,” *IEEE J. Biomed. Health Inform.*, 2025.

[10] W. Du, D. Côté, and Y. Liu, “SAITS: self-attention-based imputation for time series,” *Expert Syst. Appl.*, vol. 219, p. 119619, 2023.

[11] X. Qian, T. Zhang, M. Miao, G. Xu, X. Zhang, W. Yu, and D. Chen, “Cross-modal missing time-series imputation using dense spatio-temporal transformer nets,” *Math. Biosci. Eng.*, vol. 21, no. 4, pp. 4989–5006, 2024.

[12] Y. Liu, H. Zhang, C. Li, X. Huang, J. Wang, and M. Long, “Timer: Generative pre-trained transformers are large time series models,” in *Proc. Int. Conf. Mach. Learn. (ICML)*, 2024.

[13] C. Liu, Z. Zhu, W. Hao, and G. Sun, “Heterogeneous multivariate time series imputation by transformer model with missing position encoding,” *Expert Syst. Appl.*, vol. 271, p. 126435, 2025.

[14] H. Wu, T. Hu, Y. Liu, H. Zhou, J. Wang, and M. Long, “Timesnet: Temporal 2d-variation modeling for general time series analysis,” in *Int. Conf. Learn. Represent. (ICLR)*, 2023.

[15] E. Fons, A. Sztrajman, Y. El-Laham, L. Ferrer, S. Vyetrenko, and M. Veloso, “LSCD: lomb-scargle conditioned diffusion for time series imputation,” *CoRR*, vol. abs/2506.17039, 2025.

[16] Z. Yang, H. Dong, H. Zhang, and R. Wang, “Conditional time series diffusion model for high-speed train multi-sensor signals imputation,” *IEEE Trans. Intell. Transp. Syst.*, 2025.

[17] B. Lu, Q. Miao, Y. Liu, T. S. Tamir, H. Zhao, X. Zhang, Y. Lv, and F. Wang, “A diffusion model for traffic data imputation,” *IEEE CAA J. Autom. Sinica*, vol. 12, no. 3, pp. 606–617, 2025.

[18] M. Choi and C. Lee, “Conditional information bottleneck approach for time series imputation,” in *Int. Conf. Learn. Represent. (ICLR)*, 2024.

[19] Y. Tashiro, J. Song, Y. Song, and S. Ermon, “CSDI: conditional score-based diffusion models for probabilistic time series imputation,” in *Adv. Neural Inf. Process. Syst. (NeurIPS)*, 2021, pp. 24 804–24 816.

[20] J. Zhou, J. Li, G. Zheng, X. Wang, and C. Zhou, “MTSCI: A conditional diffusion model for multivariate time series consistent imputation,” in *Proc. ACM Int. Conf. Inf. Knowl. Manag. (CIKM)*, 2024, pp. 3474–3483.

[21] Y. Chen, W. Deng, S. Fang, F. Li, N. T. Yang, Y. Zhang, K. Rasul, S. Zhe, A. Schneider, and Y. Nevymyaka, “Provably convergent schrödinger bridge with applications to probabilistic time series imputation,” in *Proc. Int. Conf. Mach. Learn. (ICML)*, vol. 202, 2023, pp. 4485–4513.

[22] X. Yang, Y. Sun, X. Yuan, and X. Chen, “Frequency-aware generative models for multivariate time series imputation,” in *Adv. Neural Inf. Process. Syst. (NeurIPS)*, 2024.

[23] H. Wang, H. Li, X. Chen, M. Gong, Z. Chen *et al.*, “Optimal transport for time series imputation,” in *Int. Conf. Learn. Represent. (ICLR)*, 2025.

[24] E. Eldele, M. Ragab, Z. Chen, M. Wu, and X. Li, “Tslanet: Rethinking transformers for time series representation learning,” in *Proc. Int. Conf. Mach. Learn. (ICML)*, 2024.

[25] R. Yang, L. Cao, J. Yang, and J. Li, “Rethinking fourier transform from A basis functions perspective for long-term time series forecasting,” in *Adv. Neural Inf. Process. Syst. (NeurIPS)*, 2024.

[26] J. W. Cooley and J. W. Tukey, “An algorithm for the machine calculation of complex fourier series,” *Math. Comput.*, vol. 19, pp. 297–301, 1965.

[27] S. Kumawat, M. Verma, Y. Nakashima, and S. Raman, “Depthwise spatio-temporal STFT convolutional neural networks for human action recognition,” *IEEE Trans. Pattern Anal. Mach. Intell.*, vol. 44, no. 9, pp. 4839–4851, 2022.

[28] Z. Zhao and G. Li, “Synchrosqueezing-based short-time fractional fourier transform,” *IEEE Trans. Signal Process.*, vol. 71, pp. 279–294, 2023.

[29] G. E. P. Box, G. M. Jenkins, G. C. Reinsel, and G. M. Ljung, “Time series analysis: Forecasting and control,” *The Statistician*, vol. 27, pp. 265–265, 1978.

[30] C. Hamzačebi, “Improving artificial neural networks’ performance in seasonal time series forecasting,” *Inf. Sci.*, vol. 178, no. 23, pp. 4550–4559, 2008.

[31] S. van Buuren and K. G. M. Groothuis-Oudshoorn, “Mice: Multivariate imputation by chained equations in r,” *J. Stat. Softw.*, vol. 45, pp. 1–67, 2011.

[32] C. Cheng, C. Chan, and Y. Sheu, “A novel purity-based k nearest neighbors imputation method and its application in financial distress prediction,” *Eng. Appl. Artif. Intell.*, vol. 81, pp. 283–299, 2019.

[33] I. B. Aydilek and A. Arslan, “A hybrid method for imputation of missing values using optimized fuzzy c-means with support vector regression and a genetic algorithm,” *Inf. Sci.*, vol. 233, pp. 25–35, 2013.

[34] D. J. Stekhoven and P. Bühlmann, “Missforest - non-parametric missing value imputation for mixed-type data,” *Bioinform.*, vol. 28, no. 1, pp. 112–118, 2012.

[35] J. Wang, W. Du, W. Cao, K. Zhang, W. Wang, Y. Liang, and Q. Wen, “Deep learning for multivariate time series imputation: A survey,” *CoRR*, vol. abs/2402.04059, 2024.

[36] J. Yoon, W. R. Zame, and M. van der Schaar, “Estimating missing data in temporal data streams using multi-directional recurrent neural networks,” *IEEE Trans. Biomed. Eng.*, vol. 66, no. 5, pp. 1477–1490, 2019.

[37] W. Cao, D. Wang, J. Li, H. Zhou, L. Li, and Y. Li, “BRITS: bidirectional recurrent imputation for time series,” in *Adv. Neural Inf. Process. Syst. (NeurIPS)*, 2018, pp. 6776–6786.

[38] Y. Luo, X. Cai, Y. Zhang, J. Xu, and X. Yuan, “Multivariate time series imputation with generative adversarial networks,” in *Adv. Neural Inf. Process. Syst. (NeurIPS)*, 2018, pp. 1603–1614.

[39] M. Khayati, A. Lerner, Z. Tymchenko, and P. Cudré-Mauroux, “Mind the gap: An experimental evaluation of imputation of missing values techniques in time series,” *Proc. VLDB Endow.*, vol. 13, no. 5, pp. 768–782, 2020.

[40] V. Fortuin, D. Baranchuk, G. Rätsch, and S. Mandt, “GP-VAE: deep probabilistic time series imputation,” in *Int. Conf. Artif. Intell. Stat. (AISTATS)*, vol. 108, 2020, pp. 1651–1661.

[41] Z. Wu, S. Pan, G. Long, J. Jiang, and C. Zhang, “Graph wavenet for deep spatial-temporal graph modeling,” in *Proc. Int. Joint Conf. Artif. Intell. (IJCAI)*, 2019, pp. 1907–1913.

[42] P. Bansal, P. Deshpande, and S. Sarawagi, “Missing value imputation on multidimensional time series,” *Proc. VLDB Endow.*, vol. 14, no. 11, pp. 2533–2545, 2021.

[43] A. Cini, I. Marisca, and C. Alippi, “Filling the g\_ap\_s: Multivariate time series imputation by graph neural networks,” in *Int. Conf. Learn. Represent. (ICLR)*, 2022.

[44] I. Marisca, A. Cini, and C. Alippi, “Learning to reconstruct missing data from spatiotemporal graphs with sparse observations,” in *Adv. Neural Inf. Process. Syst. (NeurIPS)*, 2022.

[45] A. Vaswani, N. Shazeer, N. Parmar, J. Uszkoreit, L. Jones, A. N. Gomez, L. Kaiser, and I. Polosukhin, “Attention is all you need,” in *Adv. Neural Inf. Process. Syst. (NeurIPS)*, 2017, pp. 5998–6008.

[46] Q. Wen, T. Zhou, C. Zhang, W. Chen, Z. Ma, J. Yan, and L. Sun, “Transformers in time series: A survey,” in *Proc. Int. Joint Conf. Artif. Intell. (IJCAI)*, 2023, pp. 6778–6786.

[47] S. Liu, X. Li, G. Cong, Y. Chen, and Y. Jiang, “Multivariate time-series imputation with disentangled temporal representations,” in *Int. Conf. Learn. Represent. (ICLR)*, 2023.

[48] T. Nie, G. Qin, W. Ma, Y. Mei, and J. Sun, “Imputeformer: Low rankness-induced transformers for generalizable spatiotemporal imputation,” in *Proc. ACM SIGKDD Int. Conf. Knowl. Discov. Data Min. (KDD)*, 2024, pp. 2260–2271.

[49] B. Jing, D. Zhou, K. Ren, and C. Yang, “Causality-aware spatiotemporal graph neural networks for spatiotemporal time series imputation,” in *Proc. ACM Int. Conf. Inf. Knowl. Manag. (CIKM)*, 2024, pp. 1027–1037.

[50] G. Liang, P. Tiwari, S. Nowaczyk, and S. Byttner, “Higher-order spatiotemporal physics-incorporated graph neural network for multivariate time series imputation,” in *Proc. ACM Int. Conf. Inf. Knowl. Manag. (CIKM)*, 2024, pp. 1356–1366.

[51] X. Wang, H. Zhang, P. Wang, Y. Zhang, B. Wang, Z. Zhou, and Y. Wang, “An observed value consistent diffusion model for imputing missing values in multivariate time series,” in *Proc. ACM SIGKDD Int. Conf. Knowl. Discov. Data Min. (KDD)*, 2023, pp. 2409–2418.

[52] X. Yuan and Y. Qiao, “Diffusion-ts: Interpretable diffusion for general time series generation,” in *Int. Conf. Learn. Represent. (ICLR)*, 2024.

[53] M. Liu, H. Huang, H. Feng, L. Sun, B. Du, and Y. Fu, “Pristi: A conditional diffusion framework for spatiotemporal imputation,” in *IEEE Int. Conf. Data Eng. (ICDE)*, 2023, pp. 1927–1939.

[54] A. W. Mulyadi, E. Jun, and H. Suk, “Uncertainty-aware variational-recurrent imputation network for clinical time series,” *IEEE Trans. Cybern.*, vol. 52, no. 9, pp. 9684–9694, 2022.

[55] S. Kim, H. Kim, E. Yun, H. Lee, J. Lee, and J. Lee, “Probabilistic imputation for time-series classification with missing data,” in *Proc. Int. Conf. Mach. Learn. (ICML)*, vol. 202, 2023, pp. 16 654–16 667.

[56] Y. Liu, R. Yu, S. Zheng, E. Zhan, and Y. Yue, “NAOMI: non-autoregressive multiresolution sequence imputation,” in *Adv. Neural Inf. Process. Syst. (NeurIPS)*, 2019, pp. 11 236–11 246.

- [57] X. Miao, Y. Wu, J. Wang, Y. Gao, X. Mao, and J. Yin, “Generative semi-supervised learning for multivariate time series imputation,” in *AAAI Conf. Artif. Intell. (AAAI)*, 2021, pp. 8983–8991.
- [58] Y. Yang, M. Jin, H. Wen, C. Zhang, Y. Liang, L. Ma, Y. Wang, C. Liu, B. Yang, Z. Xu, J. Bian, S. Pan, and Q. Wen, “A survey on diffusion models for time series and spatio-temporal data,” *CoRR*, vol. abs/2404.18886, 2024.
- [59] J. M. L. Alcaraz and N. Strodthoff, “Diffusion-based time series imputation and forecasting with structured state space models,” *Trans. Mach. Learn. Res.*, vol. 2023, 2023.
- [60] Z. Dai, E. J. Getzen, and Q. Long, “SADI: similarity-aware diffusion model-based imputation for incomplete temporal EHR data,” in *Int. Conf. Artif. Intell. Stat. (AISTATS)*, vol. 238, 2024, pp. 4195–4203.
- [61] J. B. Allen and L. R. Rabiner, “A unified approach to short-time fourier analysis and synthesis,” *Proc. IEEE*, vol. 65, no. 11, pp. 1558–1564, 1977.
- [62] J. Shi, J. Zheng, X. Liu, W. Xiang, and Q. Zhang, “Novel short-time fractional fourier transform: Theory, implementation, and applications,” *IEEE Trans. Signal Process.*, vol. 68, pp. 3280–3295, 2020.
- [63] V. Namias, “The fractional order fourier transform and its application to quantum mechanics,” *IMA J. Appl. Math.*, vol. 25, no. 3, pp. 241–265, 1980.
- [64] I. Daubechies, J. Lu, and H. Wu, “Synchrosqueezed wavelet transforms: An empirical mode decomposition-like tool,” *Appl. Comput. Harmon. Anal.*, vol. 30, no. 2, pp. 243–261, 2011.
- [65] J. Sohl-Dickstein, E. A. Weiss, N. Maheswaranathan, and S. Ganguli, “Deep unsupervised learning using nonequilibrium thermodynamics,” in *Proc. Int. Conf. Mach. Learn. (ICML)*, vol. 37, 2015, pp. 2256–2265.
- [66] J. Ho, A. Jain, and P. Abbeel, “Denoising diffusion probabilistic models,” in *Adv. Neural Inf. Process. Syst. (NeurIPS)*, 2020.
- [67] H. Zhou, S. Zhang, J. Peng, S. Zhang, J. Li, H. Xiong, and W. Zhang, “Informer: Beyond efficient transformer for long sequence time-series forecasting,” in *AAAI Conf. Artif. Intell. (AAAI)*, 2021, pp. 11 106–11 115.
- [68] Y. Li, R. Yu, C. Shahabi, and Y. Liu, “Diffusion convolutional recurrent neural network: Data-driven traffic forecasting,” in *Int. Conf. Learn. Represent. (ICLR)*, 2018.
- [69] J.-B. Lugagne, C. M. Blassick, and M. J. Dunlop, “Deep model predictive control of gene expression in thousands of single cells,” *Nat. Commun.*, vol. 15, no. 1, p. 2148, 2024.
- [70] R. J. Hyndman and A. B. Koehler, “Another look at measures of forecast accuracy,” *Int. J. Forecast.*, vol. 22, no. 4, pp. 679–688, 2006.
- [71] S. Makridakis, “Accuracy measures: theoretical and practical concerns,” *Int. J. Forecast.*, vol. 9, no. 4, pp. 527–529, 1993.
- [72] T. Gneiting and A. E. Raftery, “Strictly proper scoring rules, prediction, and estimation,” *J. Am. Stat. Assoc.*, vol. 102, no. 477, pp. 359–378, 2007.
- [73] S. Wang, H. Wu, X. Shi, T. Hu, H. Luo, L. Ma, J. Y. Zhang, and J. Zhou, “Timemixer: Decomposable multiscale mixing for time series forecasting,” in *Int. Conf. Learn. Represent. (ICLR)*, 2024.
- [74] S. Wang, J. Li, X. Shi, Z. Ye, B. Mo, W. Lin, S. Ju, Z. Chu, and M. Jin, “Timemixer++: A general time series pattern machine for universal predictive analysis,” in *Int. Conf. Learn. Represent. (ICLR)*, 2025.